Materials Advances

ROYAL SOCIETY OF CHEMISTRY

PAPER

View Article Online
View Journal

Cite this: DOI: 10.1039/d6ma00088f

Design of experiments guided hydrothermal synthesis of $CuFeO_2$ photocathodes for photoelectrochemical hydrogen evolution

Mohamed El Idrissi,[ab] Jonathan Pöttker-Menke,[a] Ying Kong,[a] Mohammed Abd-Lefdil,[b] Lahoucine Atourki[b] and Bastian Timo Mei*[a]

Received 20th January 2026,
Accepted 4th May 2026

DOI: 10.1039/d6ma00088f

rsc.li/materials-advances

The development of photocathodes exhibiting sufficient stability, strong visible light absorption, and the capacity to generate high photovoltages is essential for the success of photoelectrochemical hydrogen production. In this study, we report the synthesis and characterisation of $CuFeO_2$ photocathodes *via* a one-step hydrothermal deposition process, guided by Design of Experiments (DoE) methodologies. The synthesis parameters, including hydrothermal temperature, hydrothermal time, annealing temperature, and annealing time, were systematically optimised through a Box-Behnken design. Phase pure $CuFeO_2$ delafossite was obtained, following optimized hydrothermal synthesis at 110 °C for 1 h and annealing at 650 °C for 1 h. The optimized $CuFeO_2$ photoelectrodes delivered a photocurrent density of 1.7 mA cm^{-2} at 0.4 V *vs.* RHE under 1 sun illumination in N_2-purged 1 M NaOH. Crucially, H_2 evolution was observed and quantified (faradaic efficiency of 40%). Thus, the proposed approach, integrating a one-step hydrothermal synthesis with statistical optimisation, represents the first validation of PEC H_2 production from $CuFeO_2$ photocathodes. Still persistent self-reduction under strongly cathodic bias was not inhibited. Overall, this study establishes a pragmatic, statistically guided pathway for enhancing the efficiency of $CuFeO_2$-based photocathodes, thereby addressing practical limitations typically associated with $CuFeO_2$ materials.

Introduction

The global energy crisis and environmental pollution have intensified the demand for technologies that can effectively harness solar energy, a clean and abundant resource.[1,2] Photoelectrochemical (PEC) water splitting is a promising approach to convert solar energy into storable and transportable hydrogen fuel. For efficient water splitting, a PEC device must generate a photovoltage of at least 1.7 V using one photoabsorber or tandem absorber devices.[3] Tandem PEC cells, which combine an n-type semiconductor photoanode for water oxidation ($H_2O \rightarrow O_2$) and a p-type semiconductor photocathode for water reduction ($H^+ \rightarrow H_2$), are particularly attractive options. These cells have been shown to enable bias-free water splitting under sunlight,[4–7] which is a prerequisite for economic competitiveness with fossil fuel-based hydrogen production methods.[8,9] However, current lab-scale solar-to-hydrogen (STH) conversion efficiencies for such systems remain low, typically around 1%.[10,11]

While significant progress has been made in developing n-type photoanodes (*e.g.*, WO_3, Fe_2O_3, $BiVO_4$[12]) identifying suitable p-type photocathode materials remains a challenge.[13–17] Materials like p-Si and copper-based compounds (*e.g.*, p-Cu_2O,[16,18,19] p-$CuGaSe_2$,[20] p-Cu_2ZnSnS_4[21,22]) have shown promise due to their high photoactivity and abundance. However, issues such as energy-intensive fabrication processes or the need for (toxic) protective overlayers (*e.g.*, CdS) due to an inherently poor stability,[16,19,22–25] complicate production and increases costs, highlighting the need for intrinsically stable p-type materials for water photoreduction. While surface-modified polycrystalline Cu-based photocathodes can indeed deliver high photocurrents, faradaic efficiencies and improved stability when protected, many of those gains rely on additional, complex processing (vacuum or epitaxial growth, thin-film deposition) or sacrificial/oxygenated testing conditions that are not directly comparable to scavenger-free operation. In this context, p-type delafossite materials have emerged as promising candidates for photocathodes. Delafossites ($CuMO_2$, M = Cr, Al, Fe, Ga, Rh)[26–31] have been extensively studied for applications in catalysis,[32–36] sensors,[37] magnetic

---

[a] *Laboratory of Industrial Chemistry, Ruhr-University Bochum, Universitätsstraße 150, 44801 Bochum, Germany. E-mail: bastian.mei@rub.de*

[b] *MANAPSE Lab, Faculty of Science, Mohammed V University in Rabat, avenue Ibn Batouta, P.B. 1014, Rabat, Morocco*

semiconductors,[38–40] light-emitting diodes,[41] and transparent p-type conducting oxides (p-TCOs).[42,43] $CuFeO_2$,[29] in particular, exhibits favourable properties for water reduction, including a suitable bandgap ($\sim$1.5 eV),[29,44] high absorption coefficient ($\sim 10^7$ cm^{-1}), a favourable onset potential ($\sim$1.0 V *vs.* RHE),[45] and stability in aqueous environments. Its conduction band position ($\sim$0.4 V *vs.* RHE) is well-suited for water reduction,[46] and its p-type conductivity arises from Cu vacancies and interstitial oxygen in its crystalline structure.[47] Despite these advantages, for $CuFeO_2$ only modest photocurrents under inert conditions have been demonstrated. For example $\sim$25 μA cm^{-2} at +0.4 V *vs.* RHE in an Ar-purged 1 M NaOH[45] have been reported as well as photocurrents of around $\sim$100 μA cm^{-2} in recent thin-film studies.[48] Importantly hydrogen evolution has not yet been convincingly revealed.[49]

Traditional synthesis methods for $CuFeO_2$, such as solid-state reactions or sol–gel processes, require high temperatures (800–1200 °C) and inert atmospheres.[50–53] This generally limits the potential for optimising the material and also makes these methods unsuitable for large-scale production. Alternative methods, such as hydrothermal synthesis, have gained attention due to their lower temperature requirements, environmental friendliness, and ability to produce high-purity materials with controllable morphologies.[51,54,55] A direct hydrothermal route for the fabrication of $CuFeO_2$ films even allows for one-step growth of adherent films suitable for photoelectrochemical applications and testing.[56] This one step hydrothermal synthesis route also offers a practical pathway to mitigate common limitations of $CuFeO_2$.[57,58] Still a statistically rigorous synthesis optimization has not yet been performed.

Thus, in this study, we used Design of Experiments (DoE) guided hydrothermal synthesis approach to grow crystalline phase-pure $CuFeO_2$ films directly on fluorine-doped tin oxide (FTO) substrates. Using a Box-Behnken design (BBD) coupled with the analysis of variance (ANOVA), we systematically optimised the synthesis conditions for photoelectrochemical currents of the bare (unmodified) $CuFeO_2$ films. In comparison with conventional trial-and-error methodologies, this DoE approach provides a statistically robust framework to explore the multi-variable interactions of the synthesis strategy with a reduced number of experiments, ultimately enhancing the activity of bare $CuFeO_2$ photocathodes. Our optimized phase-pure $CuFeO_2$ films demonstrated photocurrents of 2.7 mA cm^{-2} at +0.4 V *vs.* RHE in oxygen-purged 1 M NaOH and 1.7 mA cm^{-2} at +0.4 V *vs.* RHE in N_2-purged 1 M NaOH. Gas chromatography performed during controlled chronoamperometry verified photoelectrochemical H_2 evolution at a faradaic efficiency of 40%. To our knowledge, this is the first confirmed report of PEC H_2 production from $CuFeO_2$ photocathodes in N_2-purged alkaline electrolyte.

Experimental section

Reagents and materials

Copper(II) sulphate pentahydrate ($CuSO_4{\cdot}5H_2O$, 99.5%, Sigma-Aldrich), iron(II) sulphate heptahydrate ($FeSO_4{\cdot}7H_2O$, 99.0%, Sigma-Aldrich), and urea (99.0%, Sigma-Aldrich) were used as received. The aqueous solution for the hydrothermal reaction was prepared using HPLC-grade water. Fluorine-doped tin oxide (FTO) glass slides with a sheet resistance of $\sim$7 Ω sq^{-1} (Sigma-Aldrich) were used as substrates.

Hydrothermal synthesis of $CuFeO_2$

The hydrothermal synthesis of $CuFeO_2$ thin films was conducted on fluorine-doped tin oxide (FTO) glass substrates, using a modified version of a previously reported method (see Fig. 1).[59] In short, $CuFeO_2$ films were grown on a thoroughly cleaned FTO substrate (1 cm × 2 cm), which was placed FTO-side down in the PTFE liner of the hydrothermal vessel, using aqueous solutions of copper(II) sulphate ($CuSO_4$), iron(II) sulphate ($FeSO_4$) and urea (step 1). After the hydrothermal reaction, the FTO substrates were rinsed with deionized

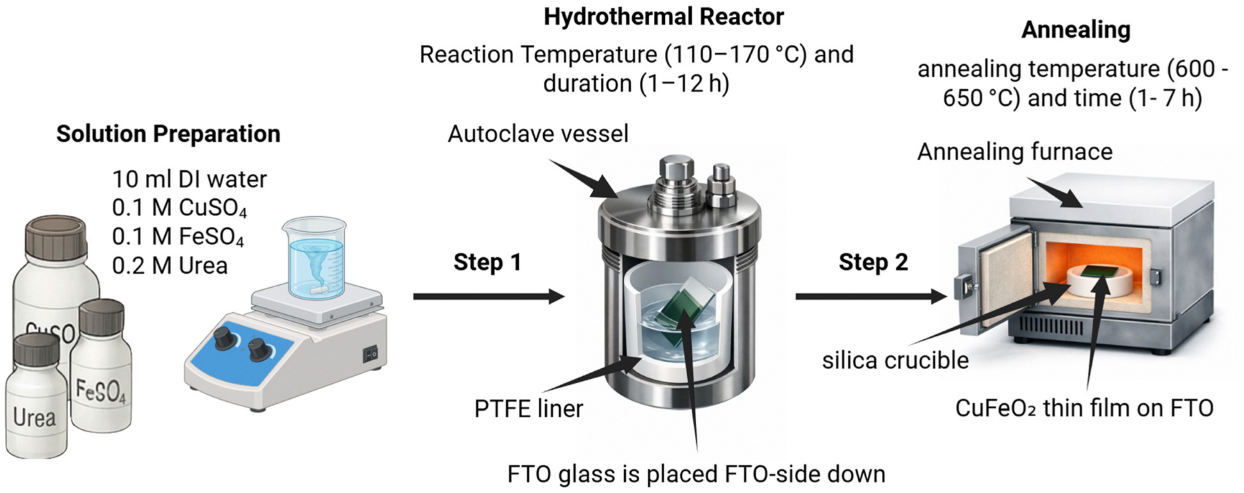

Fig. 1 Schematic representation of the hydrothermal synthesis process for $CuFeO_2$ on FTO glass substrates.

water, dried, and annealed to obtain high-quality $CuFeO_2$ films (step 2). To systematically investigate the influence of synthesis parameters on the photoelectrochemical (PEC) performance of $CuFeO_2$ photocathodes, a DoE approach was employed using the Box-Behnken design (BBD). Four key synthesis parameters were selected as independent variables: hydrothermal synthesis temperature, hydrothermal synthesis time, annealing temperature, and annealing time. The design space was constructed to explore the linear, interaction, and quadratic effects of these variables on the photocurrent density. A total of 25 experiments were generated and executed based on the BBD matrix. The experimental data were analysed using the DoE (Pro) app in OriginLab, which integrates statistical modelling and graphical analysis tools. The app utilizes R-based packages (*e.g.*, rsm, FrF2, qpcR) to fit response surface models, perform ANOVA, and visualize factor interactions through contour plots, surface plots, and desirability maps. Response surface regression analysis was applied to fit a quadratic model correlating synthesis parameters with photocurrent density. The model was validated using diagnostic plots and statistical metrics, including R^2, adjusted R^2, and variance inflation factors (VIF), confirming the absence of multicollinearity and the robustness of the predictive model. Optimization was performed using the built-in response optimizer in Origin, which identified the synthesis conditions yielding the highest photocurrent density. A validation experiment conducted under the optimized conditions confirmed the predicted photocurrent density, demonstrating the effectiveness of the BBD-guided optimization strategy.

Sample characterization

The crystalline structure and phase purity of the hydrothermally synthesized $CuFeO_2$ powders were investigated using X-ray diffraction (XRD). Measurements were performed on a Bruker D8 ADVANCE diffractometer equipped with a Cu Kα radiation source (λ = 0.1542 nm), operating in reflection geometry. The diffraction patterns were recorded over a 2θ range of 20° to 80° with a step size of 0.02°, using zero-background sample holders to accommodate small powder quantities.

Transmission electron microscopy (TEM) and scanning TEM (STEM) imaging (bright-field BF and high-angle annular dark-field HAADF) were performed using a JEOL JEM-2800 microscope equipped with a Schottky field emission cathode, operated at an accelerating voltage of 200 kV. Elemental mapping was conducted using dual silicon drift detectors (SDD) with a combined solid angle of 0.95 srad and a spectral resolution of 133 eV. The point-to-point resolution of the microscope is 0.2 nm, with an information limit of 0.09 nm, enabling detailed lattice imaging and phase identification. For TEM measurement 10 mg of $CuFeO_2$ powder was dispersed in 300 μL of ethanol and 5 μL of Nafion solution. After sonication and centrifugation a small aliquot of the supernatant was drop-cast onto a carbon-coated gold grid and dried under ambient conditions.

Scanning electron microscopy (SEM) and energy-dispersive X-ray spectroscopy (EDX) were conducted using a Zeiss Merlin Gemini II field-emission scanning electron microscope (FE-SEM), equipped with a Schottky field emitter and operated at an accelerating voltage of 5–15 kV. A thin carbon coating to prevent charging effects and ensure accurate imaging and quantification was applied with a Cressington 208 carbon device before measurement.

The optical properties of the optimized $CuFeO_2$ thin-film photocathode were investigated using UV-vis spectroscopy. Absorbance measurements in the UV-vis range (200–900 nm) were performed using a PKI 100 mm integrating sphere accessory coupled to a PerkinElmer Lambda 650 spectrophotometer. Due to instrumental limitations, measurements beyond 900 nm could not be acquired using the integrating sphere. To extend the spectral analysis into the visible-near infrared (Vis-NIR) region, standard transmission mode measurements were performed. Spectra were recorded at room temperature, and baseline corrections were applied using a FTO substrate. The absorption data were processed using the Tauc plot method to estimate the optical band gap.

X-ray photoelectron spectroscopy (XPS) were carried out using a Kratos Axis Supra spectrometer equipped with a monochromatic Al Kα X-ray source ($h\nu$ = 1486.68 eV) under ultra-high vacuum conditions (base pressure $< 10^{-9}$ mbar). Survey scans and high-resolution spectra were collected for Cu 2p, Fe 2p, and O 1s regions, with binding energies calibrated against the C 1s peak at 284.8 eV. Data evaluation was performed using CasaXPS, applying Shirley background subtraction and Gaussian–Lorentzian peak fitting.

(Photo) electrochemical measurements

Photoelectrochemical measurements were conducted to evaluate the activity and stability of the optimized $CuFeO_2$ photocathode. After hydrothermal deposition, the entire 1 × 2 cm FTO substrate was uniformly coated with $CuFeO_2$. To establish electrical contact with the potentiostat, a 1 × 1 cm section of the $CuFeO_2$ layer was carefully removed, exposing the underlying conductive FTO. PEC measurements were performed in a three-electrode configuration using a Metrohm Autolab multichannel potentiostat a low-profile Ag/AgCl electrode (Pine Research, 60 mm, sealed with 4 M KCl gel), and a homemade platinum wire (2 × 2 cm) as the counter electrode. All measurements were carried out in 1 M NaOH (pH = 13.8), which was purged with high-purity N_2 for 30 minutes prior to testing to eliminate dissolved oxygen and suppress parasitic reactions. Linear sweep voltammetry (LSV) was recorded from 0 to −0.65 V *vs.* Ag/AgCl (equivalent to +1.00 to +0.35 V *vs.* RHE) under chopped illumination (50 mV light-on/50 mV light-off intervals) using a MAX-303 Xenon lamp (300 W, Asahi Spectra Co., Ltd), equipped with a collimator lens and a filter wheel (Fig. S1). Prior to measurements, the lamp was calibrated to deliver 1 sun illumination (100 mW cm^{-2}) at the sample surface using a certified reference photodiode (Thorlabs), ensuring consistency and comparability with literature-reported PEC data. The active area of the photocathode was defined as 1 cm^2, and all current densities were normalized accordingly.

Electrochemical impedance spectroscopy (EIS) was employed to investigate the charge transfer dynamics and interfacial properties of the optimized $CuFeO_2$ photocathode. Impedance data were recorded over a frequency range of 10 Hz to 100 kHz under both dark and illuminated conditions using the set-up described above for PEC measurements. Mott–Schottky analysis was performed using two fixed frequencies (5 kHz and 10 kHz) under dark conditions to determine the flat-band potential and carrier density. The Mott–Schottky relationship applied:

$$\frac{1}{{C_{\mathrm{SC}}}^2} = -\frac{2}{e\varepsilon_{\mathrm{r}}\varepsilon_0 N_{\mathrm{A}} {A_{\mathrm{s}}}^2}\left(E - E_{\mathrm{FB}} + \frac{KT}{e}\right) \tag{1}$$

where C_{SC} is the space-charge capacitance, ε is the dielectric constant (assumed 20 for $CuFeO_2$), ε is the vacuum permittivity, e is the elementary charge, N_A is the acceptor density, E is the applied potential, E_{FB} is the flat-band potential, k is Boltzmann's constant, T is the temperature, and A is the electrode area.

The measurements were conducted in 1 M NaOH electrolyte (pH = 13.8), purged with high-purity N_2 gas to eliminate dissolved oxygen. The capacitance values were extracted from the impedance data and plotted as $1/C^2$ *versus* applied potential, with the linear region fitted to extract semiconductor parameters. The impedance data were fitted using a two-time-constant equivalent circuit model of the form:

$$Z(\omega) = R_0 + (R_1||\mathrm{CPE}_1) + (R_2||\mathrm{CPE}_2)$$

where R_0 represents the uncompensated solution resistance, and the two parallel $R||$CPE elements capture fast and slow relaxation processes. This model was selected to account for both interfacial and bulk transport phenomena. All impedance spectra were acquired at 0.4 V *vs.* RHE in 1 M NaOH in the dark and under illumination (1 sun).

To evaluate the spectral response and quantum efficiency of the optimized $CuFeO_2$ photocathode, wavelength-dependent photocurrent measurements were performed using a photoelectrochemical measurement system (Instytut Fotonowy, ver. 5.3). The FTO/$CuFeO_2$ photocathode was used as working electrode (exposed active area of $(0.9/2)^2\pi$ cm^2). A platinum wire, and a low-profile Ag/AgCl (4 M KCl gel) served as the counter electrode and reference electrode, respectively. The electrolyte was 1 M NaOH (pH = 13.8), purged with high-purity N_2 gas prior to measurement to eliminate dissolved oxygen and suppress side reactions. Wavelength-dependent photocurrent measurements were conducted under monochromatic illumination across the spectral range of 400–900 nm. The incident light was modulated using an internal shutter and filter wheel, and the intensity was calibrated using a photodiode positioned at the rear of the PEC cell. Absorbed photon-to-current efficiency (APCE) was determined by dividing the IPCE by the absorptance (λ), see eqn (2), which was measured using a calibrated integrating sphere.

$$\mathrm{APCE}(\lambda) = \frac{\mathrm{IPCE}(\lambda)}{A(\lambda)} \tag{2}$$

Scanning photoelectrochemical microscopy (SPECM) was employed to spatially resolve the photoelectrochemical activity of the optimized $CuFeO_2$ photocathode. The measurements were performed using a commercial SECM system from Sensolytics GmbH (Bochum, Germany), equipped with a Metrohm Autolab multichannel potentiostat and a three-axis micromanipulator (Owis GmbH) for precise tip positioning. The system was operated *via* a custom Visual Basic 6.0 interface for scan control and data acquisition. A 25 μm diameter gold microelectrode was used as the SECM tip, serving both as a localized light source and as an electrochemical probe. The tip was coupled to a 150 W Hg–Xe lamp (Hamamatsu LC8) *via* a HITRONIC POF Simplex PE optical fiber, allowing the glass sheath of the microelectrode to act as a light guide for focused illumination of the sample surface. The tip was polished to achieve an RG value of approximately 8, ensuring efficient light transmission and spatial resolution. The $CuFeO_2$ photocathode was mounted in a Teflon SECM cell sealed with an O-ring, exposing an active area of $(0.9/2)^2\pi$ cm^2. The electrolyte consisted of 5 mM potassium ferricyanide and 100 mM KCl, selected to probe charge transfer dynamics at the illuminated surface. Prior to scanning, the tip was positioned at a fixed distance from the sample using z-approach curves recorded in air-saturated buffer. Area scans were then performed under dark and illuminated conditions, with the sample biased at a potential relevant to its photoelectrochemical operation. The tip current and sample photocurrent were recorded simultaneously to generate spatial maps of local activity.

Controlled potential chronoamperometry (1 h, +0.5 V *vs.* RHE) was used to verify light driven H_2 formation, and quantification of hydrogen was achieved using online gas analysis performed with a GC-BID (GC-2023, Shimadzu) equipped with Hayeseq *Q* and molecular sieve 13× columns. The N_2 flow (99.999%, Air Liquide, 20 mL min^{-1}) into the reactor was controlled by a mass flow controller (Bronkhorst) and delivered through a frit to ensure efficient distribution; the reactor outlet stream was sampled periodically. H_2 quantification was performed by external calibration with certified gas standards, and GC sampling was synchronized with the electrochemical measurements to calculate faradaic efficiency from the integrated H_2 evolution via:

$$\mathrm{FE} = \frac{2.F.n_{\mathrm{H_2}}}{Q} \tag{3}$$

where F is the Faraday constant, n is the number of moles of H_2 detected, and Q is the total passed charge.

Results and discussion

During the hydrothermal process, the formation of particles or thin films of $CuFeO_2$ occurred *via* redox reactions and *in situ* hydroxy generation from urea. Particularly Fe^{2+} ions derived from $FeSO_4$ facilitated a redox reaction with Cu^{2+} ions ($Cu^{2+} + Fe^{2+} \rightarrow Cu^{+} + Fe^{3+}$), generating unstable Cu^{+} ions without the need for additional reducing agents. Urea ($(NH_2)_2CO$), included as an ammonia-release agent, decomposed upon heating to produce ammonia (NH_3) and isocyanic acid (HNCO), which reacted with water to form ammonium (NH_4^{+}) and hydroxide (OH^{-}) ions. These leads to the formation of hydroxide intermediate [$(Cu,Fe)(OH)_4$], which subsequently decomposed into $CuFeO_2$ and water. The use of a mildly acidic urea solution (pH 3.9) was found to be critical, as it promoted nucleation and deposition of the thin films compared to highly alkaline conditions, which caused fine particle suspensions that hindered nucleation on the substrate surface. The presence of Fe^{2+} ensured that the pH remained within the optimal range for the synthesis process, thereby preventing any potential instability caused by excess acidity.

Validation of hydrothermal synthesis conditions

To establish a reliable baseline for the synthesis of phase-pure delafossite $CuFeO_2$, the influence of hydrothermal temperature on the material's structural, morphological, and compositional properties was systematically investigated. Therefore, $CuFeO_2$ powders were synthesized in the absence of FTO glass at hydrothermal temperatures of 110 °C, 140 °C, and 170 °C (1 hour) and characterized using X-ray diffraction (XRD), high-resolution transmission electron microscopy (HRTEM), scanning electron microscopy (SEM), and energy-dispersive X-ray spectroscopy (EDX). XRD analysis (Fig. 2a) confirmed formation of the delafossite phase, with diffraction patterns primarily indexed to the rhombohedral 3R-$CuFeO_2$ polytype (ICDD 01-075-2146). Both the 110 °C and 140 °C samples are essentially phase-pure 3R-$CuFeO_2$. The powder synthesized at 170 °C shows a more pronounced contribution from a second phase assigned to hematite α-Fe_2O_3 (ICDD 00-033-0664), indicating partial oxidation or decomposition at the highest synthesis temperature. The powders obtained at 110 °C and 140 °C exhibit the highest phase purity, characterized by sharp, intense reflections with no detectable secondary phases. A temperature dependent evolution in preferred orientation is observed: the (012) diffraction signal dominates at 110 °C, shifting to a dominant (110) reflection at 140 °C, consistent with a change in crystal growth dynamics (see SI for additional information, Fig. S2).

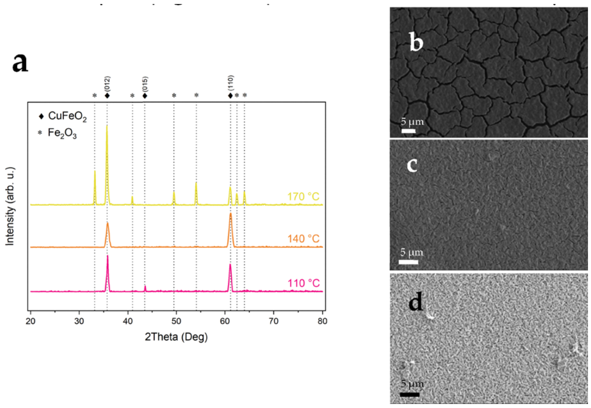

Fig. 2 (a) XRD patterns of $CuFeO_2$ powders synthesized hydrothermally at 110 °C, 140 °C, and 170 °C for 1 hour. Reference patterns for phase-pure 3R-$CuFeO_2$ (ICDD 01-075-2146) and α-Fe_2O_3 (ICDD 00-033-0664) are provided. The samples synthesized at 110 and 140 °C show high phase purity with no secondary phases. SEM top-view images of $CuFeO_2$ films grown at (b) 110 °C, (c) 140 °C, and (d) 170° after annealing at 650 °C for 1 hour. Annealing induces cracking and texturing, with films from the 140 °C and 170 °C powders exhibiting a more uniform and finely textured morphology.

The impact of synthesis temperature on particle morphology and elemental homogeneity was additionally examined by SEM and EDX. SEM imaging (Fig. S3a–c) revealed a clear morphological evolution: at 110 °C, the powder consists of smooth spherical nanoparticles; at 140 °C, the particles transform into textured spheres with surface roughening, signifying enhanced crystallization; and at 170 °C, irregular, faceted aggregates form. Elemental mapping of the 110 and 140 °C samples (Fig. S3d) demonstrates a uniform spatial distribution of Cu, Fe, and O, confirming compositional homogeneity. Quantitative EDX analysis (Fig. S4) further verified that the elemental composition (O ∼50%, Cu ∼25%, Fe ∼25%) for all samples closely matched the expected stoichiometry of $CuFeO_2$. Both 110 °C and 140 °C syntheses produce phase pure, stoichiometric 3R-$CuFeO_2$ with well-defined morphologies, representing the optimal balance of structural and compositional quality.

The morphological features observed in powders are reproduced in films grown directly by *in situ* hydrothermal deposition on FTO. Films synthesized at 110 °C form a loose, discontinuous layer with visible gaps (Fig. S5), whereas films grown at 140 °C and 170 °C develop denser, more continuous coatings with improved interparticle connectivity, indicating that higher hydrothermal temperatures promote tighter packing. Subsequent annealing at 650 °C for 1 h modifies surface texture: 110 °C films become cracked and poorly textured, while 140 °C and 170 °C films show more uniform, finely textured surfaces with regular cracking patterns (Fig. 2b–d). *In situ* hydrothermal growth therefore provides a reliable route to phase-pure delafossite $CuFeO_2$ thin films with a robust electrical contact to the FTO substrate, enabling reproducible PEC testing. In order to systematically explore the influence of synthesis parameters, a statistical optimization approach was applied. Specifically Design of Experiments using the Box-Behnken design, as detailed in the following section, was used for PEC performance optimization of the delafossite $CuFeO_2$ photocathodes.

Design of Experiments (DoE) optimization *via* Box-Behnken design of *in situ* grown $CuFeO_2$

Building upon the initial characterisation of $CuFeO_2$ powders, hydrothermal synthesis was verified to enable synthesis of phase-pure $CuFeO_2$. Thus, to optimise the full suite of synthesis parameters of *in situ* grown photocathodes on FTO glass substrates and to maximise their PEC performance, a DoE approach was employed. The complex parameter space, including the individual and interactive effects on the functional response, was explored using a Box-Behnken design, which allowed for the efficient modelling of potential nonlinear relationships with a minimised number of experimental runs. Four critical parameters were investigated (see also Table S1): hydrothermal synthesis temperature (parameter A, °C), hydrothermal synthesis time (parameter B, h), annealing temperature (parameter C, °C), and annealing time (parameter D, h). The photocurrent density (response parameter E, in mA cm^{-2}) at 0.4 V *vs.* RHE, measured under 1 sun illumination in N_2-purged 1 M NaOH electrolyte, was chosen as the response variable to quantify PEC performance. The experimental matrix and corresponding photocurrent densities for all 25 samples are provided in Table S1. A response surface regression analysis was performed on the data. Although a full quadratic model was fitted, statistical analysis of variance (ANOVA) revealed that the PEC response was overwhelmingly governed by linear effects. Additionally it was determined that all quadratic and two-factor interaction terms are statistically insignificant (p = 1.000), with coefficients being effectively zero (see Table S2). Consequently, a simplified linear model was adopted, described by the following regression equation (eqn (4), in uncoded units):

$$E = -1.68263 + 0.010997A + 0.044106B - 0.002192 \tag{4}$$

This equation was used to predict the PEC response and optimise the synthesis further. As shown in Fig. 3, there is good agreement between the experimental and predicted values for the response parameter E, suggesting that the model accurately captures the response behaviour. The model fits the experimental data exceptionally well, with coefficients of determination (R^2) and adjusted R^2 (R^2(adj)) of 98% in both cases. While these values indicate that the model accounts for all observed variance in the response, they are a known characteristic of saturated designs with a specific structure of centre points and can reflect a highly controlled experimental system rather than overfitting in this context. The standard deviation (S) of the model error is low (4.47×10^{-6}), and the variance inflation factors (VIFs) for all predictors ranged from 1.00 to 2.21, confirming the absence of multicollinearity and the robustness of the parameter estimates Table 1. Diagnostic plots including a normal probability plot of residuals, a plot of residuals *versus* fitted values, and a Pareto chart were used to validate the model's assumptions (Fig. S6a–e). The residuals were normally distributed and randomly scattered, confirming the homoscedasticity and independence of the error terms. The Pareto chart of standardized effects (Fig. S6e) unequivocally identified hydrothermal synthesis temperature (A) as the most significant factor influencing the PEC response, followed by the duration of the hydrothermal synthesis (B) and annealing time (D). Annealing temperature (C) had a smaller, yet statistically significant influence on the response parameter. The main effects of each synthesis parameter on the PEC response are illustrated in Fig. S7.

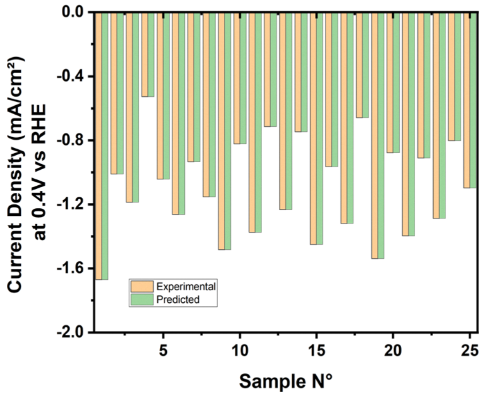

Fig. 3 Correlation between model-predicted and experimentally measured photocurrent density values at 0.4 V *vs.* RHE for the 25 $CuFeO_2$ photocathodes synthesized according to the Box-Behnken design. The perfect alignment demonstrates the exceptional predictive capability of the linear regression model.

Of particular significance is the observation that the photocurrent density becomes more negative, indicating enhanced performance for a photocathode with a decrease in hydrothermal synthesis temperature (A). This finding is consistent with the structural characterization results (Fig. 2a), which demonstrated that reduced temperatures hinder the formation of hematite impurities and promote the formation of phase-pure CuFeO2. Furthermore, a discernible hydrothermal effect on morphology is evident (see Fig. 2b–d): films synthesized at lower temperatures exhibit visible surface cracks that likely enhance electrolyte penetration and charge transfer, whereas those prepared at higher temperatures appear smoother and crack-free, correlating with reduced PEC response. The phase purity of the *in situ* grown films was also validated by Raman spectroscopy (see Fig. S8). The PEC response further improved with shorter hydrothermal synthesis time (B) and shorter annealing time (D), suggesting that prolonged processing may lead to grain coarsening or partial phase transformation. In contrast, a higher annealing temperature (C) had a positive effect on performance, likely due to enhanced crystallinity and improved interfacial contact between $CuFeO_2$ and the FTO substrate. Temperatures above 650 °C could potentially yield even higher crystallinity, however, this limit was imposed by the melting point of the FTO substrate, which constrains further thermal optimization. Thus, the performed DoE (25 runs) shows that while hydrothermal and annealing conditions strongly control photocurrent through changes in crystallinity and morphology, degradation by cathodic self-reduction is observed across the tested parameter space and cannot be

Table 1 Analysis of Variance (ANOVA) summary for the fitted linear model

Statistic	Value	Interpretation
R^2	98%	The model explains all variance in the response.
R^2 (adj)	98%	The model maintains perfect predictive power after adjusting for the number of predictors.
S	4.47×10^{-6}	The standard error of the model is extremely low.
VIF range	1.00–2.21	Predictors are independent, with no significant multicollinearity.

fully avoided under the present operating conditions, we attribute this behaviour to two linked effects: temperature-driven changes in crystallinity, grain boundaries and surface defect chemistry alter how the film responds to cathodic bias, with more defective or poorly connected microstructures being more susceptible to local reduction, and the working potential used here (+0.5 V *vs.* RHE) lies close to the thermodynamic and kinetic thresholds for Cu and Fe reduction, making partial reduction thermodynamically accessible even at relatively low applied bias. Together these factors explain why synthesis optimization improves initial photocurrent but does not eliminate progressive self-reduction during operation. The Box-Behnken model successfully identified the linear relationships between the four synthesis parameters and PEC performance, confirming that hydrothermal synthesis at 110 °C for 1 h followed by annealing at 650 °C for 1 h maximizes photocurrent density, and demonstrating that the statistical model provides a powerful, predictive framework for guiding the synthesis of higher-performance $CuFeO_2$ photoelectrodes.

Characterization of optimized $CuFeO_2$ photocathodes

The optical properties of the optimized $CuFeO_2$ photocathode was first characterized by UV-vis spectroscopy. Standard transmission measurements (Fig. S9a) exhibited a distinct absorption edge at ∼650 nm. The corresponding Tauc plot for indirect transitions (Fig. 4a) yielded an indirect bandgap of 1.58 eV. Measurements of the absorption spectrum using an integrating sphere (Fig. S9b) revealed an additional absorption edge at ∼400 nm and the associated Tauc plot (Fig. 4b) associated with a direct bandgap of 3.01 eV. This dual bandgap nature (1.58 eV indirect and 3.01 eV direct) is consistent with the material's unique electronic structure,[48,60] where the valence band comprises hybridized Fe 3d, Cu 3d, and O 2p orbitals, and the conduction band consists of Fe 3d antibonding states.[60] The high absorption coefficient ($>10^5$ cm^{-1} across the visible spectrum) confirms the material's strong capacity for visible light harvesting.

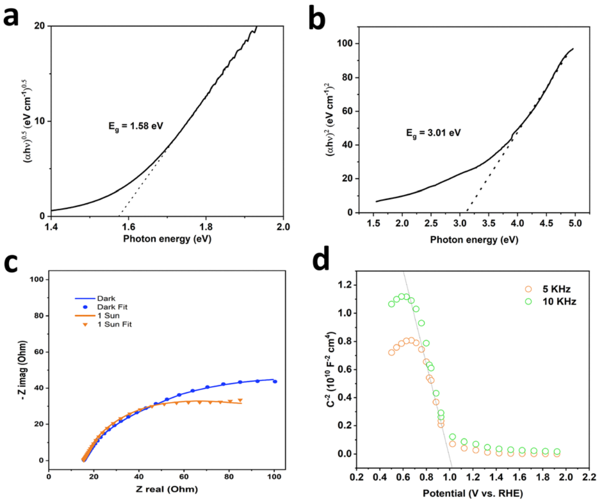

Fig. 4 Comprehensive optoelectronic characterization of the optimized $CuFeO_2$ photocathode. (a) Tauc plot showing an indirect bandgap of 1.58 eV. (b) Tauc plot from transmission data indicating a direct bandgap of 3.01 eV. (c) Nyquist plots of optimized $CuFeO_2$ photocathodes measured at 0.4 V *vs.* RHE in 1 M NaOH under dark and illuminated (1 sun) conditions. Scatter points represent fits to the two-time-constant equivalent circuit model, while solid lines show the experimental data. Fitted parameters are summarized in Table 2. (d) Mott–Schottky plot measured in the dark, confirming p-type conductivity and yielding a flat-band potential of 1.01 V *vs.* RHE.

Nyquist plots (Fig. 4c), obtained from EIS performed at 0.4 V *vs.* RHE in 1 M NaOH in the dark and under 1 sun illumination, exhibit two distinct semicircles, consistent with a dual-process relaxation behavior. The fitted curves using the two-time-constant equivalent circuit show excellent agreement with the experimental data ($R^2 > 0.99$), and the extracted parameters are summarized in Table 2. Under illumination, both R_1 and R_2 decrease significantly (from 44.62 Ω to 8.04 Ω and from 180.81 Ω to 144.66 Ω, respectively), indicating enhanced charge transfer and reduced recombination losses. The increase in CPE values under light (*e.g.*, CPE_2 from 2.10×10^{-4} F to 8.04×10^{-4} F), suggesting a narrowing of the depletion layer width and an increase in the density of photogenerated holes, consistent with improved photoactivity.[61]

Mott–Schottky plots were constructed using the impedance in the high-frequency region. These measurements were performed in the dark over a potential window of +0.4 to +1.0 V *vs.* RHE. The Mott–Schottky plot (Fig. 1d) shows a clear linear region with a negative slope, confirming the p-type conductivity of $CuFeO_2$. By linear extrapolation, a flat-band potential E_{FB} of 1.01 V *vs.* RHE was obtained in excellent agreement with literature reports.[44,45,48] This value suggests that the conduction band minimum of $CuFeO_2$ is situated above to the thermodynamic potential of the hydrogen evolution reaction (HER) and thus hydrogen production is thermodynamically feasible. Assuming a dielectric constant of 20,[44] the acceptor density N_A was calculated to be $\sim 10^{18}$ cm^{-3}, indicating a relatively high concentration of majority carriers, *i.e.* holes in this case.

Based on the combined optical and electrochemical results an energy band diagram was constructed for the optimized $CuFeO_2$ photocathode (Fig. S10). The flat-band potential (E_{FB}), determined to be 1.01 V *vs.* RHE from Mott–Schottky analysis, is characteristic of the valence band edge in p-type semiconductors, where holes are the majority carriers. Given the experimentally measured indirect bandgap of 1.58 eV, the conduction band minimum (CBM) is estimated to be at approximately −0.5 V *vs.* RHE. This places the CBM well above the hydrogen evolution potential, enabling thermodynamically favourable electron transfer for solar-driven hydrogen production. The band positions are consistent with reported work function values (∼5.2 eV).[62] The favourable band alignment, high acceptor density ($\sim 10^{18}$ cm^{-3}), and enhanced charge transfer kinetics observed under illumination underscore the suitability of $CuFeO_2$ as a photocathode for PEC water splitting.

A collection of semiconductor and EIS parameters for bare $CuFeO_2$ films prepared by different scalable routes is summarized in Table S3. All three studies consistently place the indirect optical transition in the near-infrared to visible region (≈1.1–1.6 eV) in addition to a direct optical

Table 2 Impedance fitting parameters for optimized $CuFeO_2$ photocathodes measured in 1 M NaOH at 0.4 V *vs.* RHE under dark and illuminated (1 sun) conditions. Parameters were extracted using a two-time-constant equivalent circuit model (R_0 + (R_1 ∥ CPE_1) + (R_2 ∥ CPE_2)), with values reflecting solution resistance, fast interfacial relaxation, and slower bulk/interfacial processes

Sample	R_0 (Ω)	R_1 (Ω)	R_2 (Ω)	α_1	α_2	CPE_1 (F)	CPE_2 (F)	R^2 (fit quality)
Dark	15.46	44.62	180.81	0.9067	0.5756	1.07×10^{-4}	2.10×10^{-4}	0.9986
1 sun illumination	15.36	8.04	144.66	1.00	0.686	1.37×10^{-4}	3.68×10^{-4}	0.9971

transmission at 3.1–3.3 eV. The flat band potential is anodic in all reports ($\approx$+1.0 − +1.1 V *vs.* RHE), indicating favourable band alignment for driving reduction reactions when sufficient photovoltage is generated. In our optimized hydrothermal films we additionally extract standardized EIS metrics: a light-induced decrease in charge transfer resistance from 104 Ω cm^2 (dark) to 89.2 Ω cm^2 (light), and a space-charge capacitance that increases from 7.7 μF cm^{-2} (dark) to 15 μF cm^{-2} (light). These light dependent changes are consistent with increased photogenerated carrier density and improved interfacial charge transfer under illumination. The combined comparison highlights strong agreement in band edge positions across different fabrication methods.

Photoelectrochemical performance

The PEC performance of the optimised $CuFeO_2$ photocathode was also systematically evaluated. The model predicted a maximum photocurrent density of −1.7 mA cm^{-2}, which was experimentally confirmed by linear sweep voltammetry (LSV) performed under chopped 1 sun illumination (100 mW cm^{-2}) in N_2-saturated 1 M NaOH, as shown in Fig. 5a. This close agreement validates the predictive power of the statistical

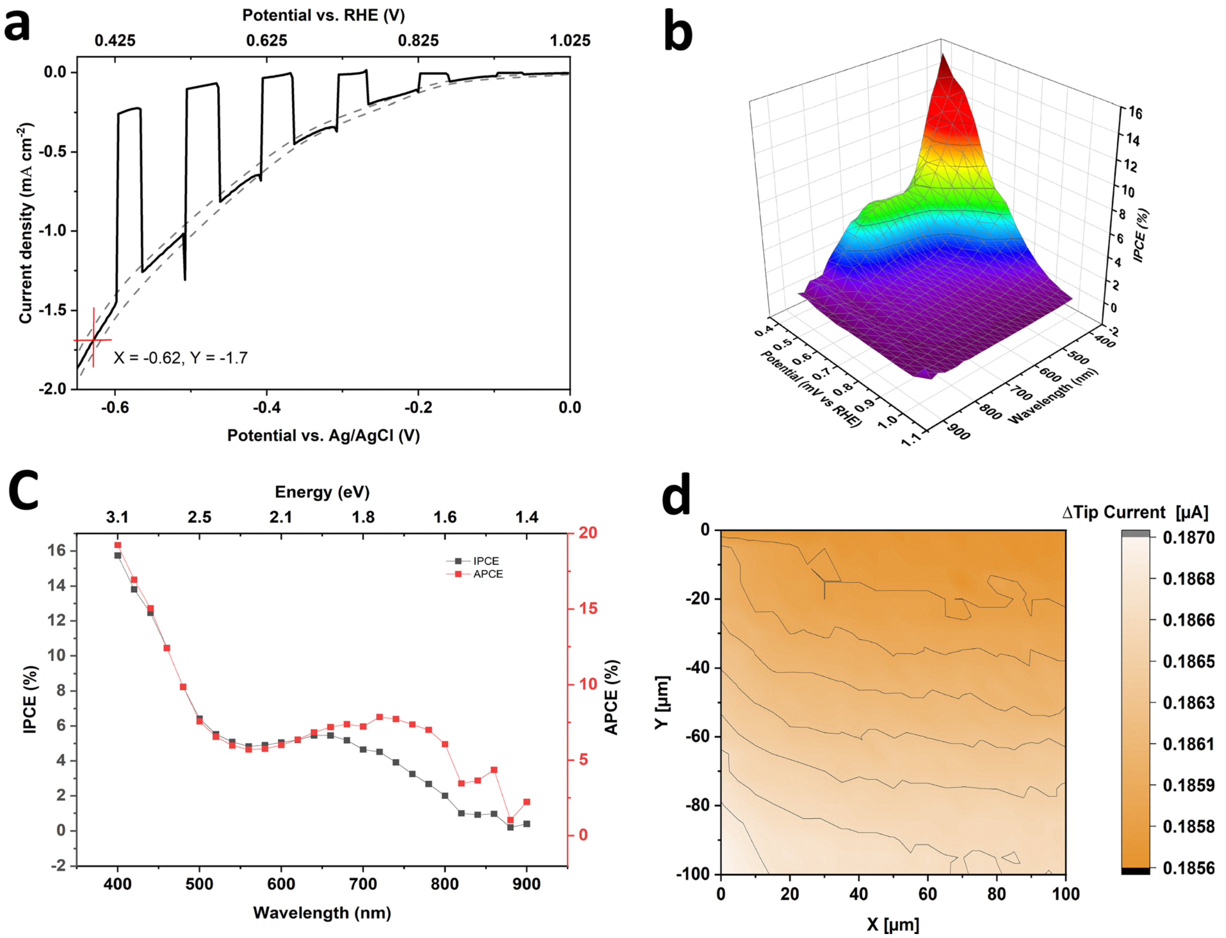

Fig. 5 Photoelectrochemical performance of the optimized $CuFeO_2$ photocathode. (a) Averaged linear sweep voltammetry (LSV) measured in N_2-saturated 1 M NaOH under chopped 1 sun illumination (100 mW cm^{-2}), confirming the predicted photocurrent density of −1.7 mA cm^{-2} at 0.4 V *vs.* RHE. The gray shaded envelope shows the minimum and maximum response from independent scans. (b) 3D plot of incident photon-to-current efficiency (IPCE) as a function of wavelength and applied potential, showing a maximum of 16% at 400 nm. (c) IPCE and absorbed photon-to-current efficiency (APCE) spectra measured at a fixed applied potential of 0.4 V *vs.* RHE. (d) Scanning photoelectrochemical microscopy (SPECM) photocurrent difference map (light–dark) showing uniform catalytic activity for Fe^{3+} reduction across the electrode surface. The sample was synthesized at 110 °C for 1 h (hydrothermal) and annealed at 650 °C for 1 h.

optimization. Moreover, the photoelectrochemical performance of the photocathode was evaluated using oxygen-saturated electrolyte (1 M NaOH). In agreement with the favourable driving force for ORR a significantly higher photocurrent density of −2.7 mA cm^{-2} was obtained at +0.4 V *vs.* RHE indicative of the material's catalytic activity for multi-electron transfer processes (Fig. S11).

To deconvolute the spectral response of the optimized films, wavelength-dependent photocurrent measurements were performed (Fig. S12). A pronounced cathodic photocurrent was observed, with distinct peaks at 400 nm (−10 μA), 650 nm (−6.2 μA), and 800 nm (−2.8 μA). This multi-wavelength response aligns with the material's dual bandgap, confirming that charge carrier generation is effective across the visible spectrum, with the most efficient absorption occurring at shorter wavelengths.

The photon conversion efficiency was further quantified by incident photon-to-current efficiency (IPCE) and absorbed photon-to-current efficiency (APCE) measurements. The 3D IPCE plot (Fig. 5b) demonstrates a strong dependence on both wavelength and applied potential, with a maximum efficiency of 16% achieved at 400 nm. Despite the decent IPCE efficiency, APCE (Fig. 5c) indicate that recombination losses are still significant. To further validate the optical and electrochemical characterization, the solar photocurrent density was estimated by numerically integrating the IPCE spectrum with the AM1.5G solar photon flux. This calculation yielded a theoretical value of −2.24 mA cm^{-2}, which exceeds the experimentally measured photocurrent of −1.7 mA cm^{-2}. This difference is primarily attributable to the use of two different illumination sources used for the individual measurements. The IPCE was recorded with using monochromatic light provided by the photoelectrochemical measurement system, while sample optimization and the corresponding LSVs were recorded with the broadband MAX-303 xenon lamp.

To probe the spatial homogeneity of the photoelectrochemical activity at the microscale, Scanning Photo electrochemical Microscopy (SPECM) was used (Fig. S13). The measurements employed a Ø 25 μm Au microelectrode tip that served both as a localized irradiation guide and as the electrochemical probe. During the measurements the Au tip was polarized at +1.5 V *vs.* RHE to drive oxidation of Fe^{2+} to Fe^{3+}. The $CuFeO_2$ photocathode was biased at +0.4 V *vs.* RHE to enable Fe^{3+} reduction and to match the PEC operating condition used for bulk measurements. Tip positioning used *z*-approach curves (Fig. S14) recorded at multiple *x*–*y* coordinates to correct for sample tilt and maintain a constant tip sample distance throughout the scan. Dark and illuminated tip currents were recorded at each grid point and the dark signal was subtracted to yield the local photocurrent difference (light–dark), which isolates photocatalytic activity related to Fe^{3+} reduction at the illuminated surface. Fig. 5d illustrates the SECM surface scan of the $CuFeO_2$ photocathode. The photocurrent increase observed under illumination was consistent with the reduction of Fe^{3+} to Fe^{2+}. Notably, the high resolution of the tip facilitates detection of microscopic regions with varying catalytic activity. However, in the case of the optimized $CuFeO_2$ photocathode, the photocurrent remained uniform across the entire scanned area, indicating excellent homogeneity of the material's surface in terms of its activity.

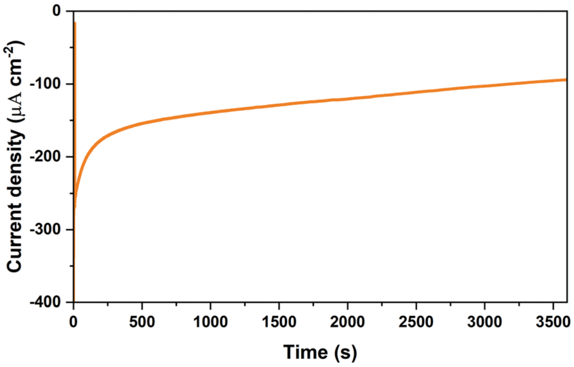

Fig. 6 Chronoamperometry (CA) recorded at +0.5 V *vs.* RHE on the optimized $CuFeO_2$ photocathode (active area 1.0 cm^2) under chopped 1 sun illumination (100 mW cm^{-2}).

Finally, chronoamperometry (CA) Fig. 6 was performed in N_2-purged 1 M NaOH at an applied potential of +0.5 V *vs.* RHE to confirm hydrogen formation. The reactor outlet was sampled periodically and analysed online using a GC with BID detector. Sampling was synchronized with the CA experiment. Illumination was toggled during the CA run to correlate light-driven current with gas production. Upon illumination, H_2 evolution was confirmed at a reproducible, steady rate of 1.036 μmol h^{-1} (Fig. S16) in the outlet stream. Notably, immediately after switching the light off the H_2 rate returned to baseline, demonstrating light-dependent H_2 generation. Integration of $n(H_2)$ as obtained from the GC analysis together with the total charge passed (Q) during the CA were used to calculate the faradaic efficiency. We obtain an average FE of 40%, confirming that a substantial fraction of the photocurrent corresponds to true, GC-verified hydrogen evolution. At the same time, post-operation XPS, SEM, visible colour change and increased macroscopic conductivity consistently indicate progressive Cu/Fe reduction after extended operation (Fig. S17–S22), thus the initial light-driven photocurrent contains a genuine hydrogen-evolution component, and partial Cu/Fe self-reduction occurs during prolonged operation and contributes to the observed decay in activity. Tables S3 and S4 compile reported performance metrics for $CuFeO_2$ photocathodes. Direct comparison is limited by differences in experimental conditions: in this work PEC tests were performed in N_2-purged 0.1 M NaOH, while several literature reports used O_2-saturated electrolytes. Gas environment and electrolyte chemistry affect measured photocurrents, side reactions and apparent faradaic efficiencies, for this reason directly comparable literature values for GC-verified FE under the same conditions are not available.[48,49] To quantify the energetic cost of hydrogen production we computed the electrical energy consumed per mole of H_2 and an estimated solar-to-hydrogen (STH) efficiency using the 1 h chronoamperometry at +0.5 V *vs.* RHE (active area

1.0 cm^2), the online GC H_2 rate and the measured faradaic efficiency ($\approx$40%). From the integrated charge and the GC-measured H_2 production (1.036 μmol h^{-1} during illumination) we obtain an electrical energy consumption of $\approx$241 kJ mol^{-1} H_2 ($\approx$33.2 kWh kg^{-1} H_2) and an estimated STH $\approx$0.068% under 1 sun illumination. These values are reported as operating-electrode metrics (they do not include additional cell or balance-of-system losses), full calculation details are provided in the SI (energy-metric calculations, Fig. S14 and S15).

Overall the optimized one-step hydrothermal films achieve the unmodified ORR photocurrent under one-sun illumination (2.7 mA cm^{-2} at +0.4 V *vs.* RHE) exceeding earlier reports and more importantly a significant HER photocurrent (1.7 mA cm^{-2} at +0.4 V *vs.* RHE) was obtained. Prévot *et al.*[45] report a photocurrent of up to $\approx$1.5 mA cm^{-2} under 1 sun illumination using sacrificial O_2 and IPCE $>$10% near 400 nm (measured at +0.4 V *vs.* RHE), but bare films produced only marginal photocurrents in the absence of oxygen unless protective coatings and catalytic overlayers (AZO/TiO_2/Pt) were applied. For $CuFeO_2$ thin films prepared by PLV Präg *et al.*[48] reported an IPCE of $\approx$12.5% at 400 nm (+0.4 V *vs.* RHE) but photocurrents remained in the μA range unless electron scavengers were used. Clearly the one-step hydrothermal synthesis combined with systematic Box-Behnken DoE optimization results in PEC properties exceeding previous reports evidencing the effectiveness of the synthesis and optimization strategy in maximizing intrinsic PEC activity.

Stability and degradation mechanisms

Despite the promising photoelectrochemical (PEC) performance, the operational stability of the optimized $CuFeO_2$ photocathode emerged as a remaining critical factor. A significant decay in photocurrent was observed under continuous operation. To elucidate the underlying degradation mechanisms, characterization was conducted using XPS, electrical conductivity measurements, and SEM on photocathodes before and after PEC testing. The chemical state of the pristine photocathode was first determined by XPS. The survey spectrum confirmed the presence of Cu, Fe, and O with no detectable impurities (Fig. S17). High-resolution scans of the Cu 2p region (Fig. 7a) exhibit a dominant Cu^+ $2p_{3/2}$ peak with a very weak satellite at $\sim$945 eV, characteristic of monovalent copper. The assignment of Cu^+ is further supported by the Cu LMM Auger spectra (Fig. 7b) which display a primary peak with a shoulder, consistent with Cu^+. The Fe 2p region (Fig. 7c) reveals spin–orbit split doublets at $\sim$710.9 eV (Fe $2p_{3/2}$) and $\sim$724.4 eV (Fe $2p_{1/2}$), with multiple splitting characteristic of high-spin Fe^{3+} in an octahedral coordination. The O 1s spectrum (Fig. 7d) showed a single, broad asymmetric peak at 532.1 eV, attributed to lattice oxygen in the delafossite structure.

Following PEC operation under cathodic bias, the electrode exhibits a distinct colour change from dark green to brown (Fig. S18), alongside an increase in electrical conductivity. Changes induced during operation were subsequently analysed by XPS. Survey spectra (Fig. S19) indicate the absence of contamination, yet substantial chemical transformations in the copper and iron states are discernible through region scans. The Cu 2p spectrum (Fig. 7e) displays two narrow peaks at 932.6 eV (Cu $2p_{3/2}$) and 952.5 eV (Cu $2p_{1/2}$), without satellite features. These results conclusively indicate the formation of metallic copper (Cu^0). This finding is further supported by the Cu LMM Auger spectrum (Fig. 7f), which shows a dominant peak at a kinetic energy of $\sim$918.6 eV. In the Fe $2p_{3/2}$ region scan (Fig. 7g) the emergence of satellite peaks at $\sim$715 and $\sim$731 eV is noted, indicating partial reduction of Fe^{3+} to Fe^{2+}. This suggests that not only Cu^+ but also Fe^{3+} undergoes redox transformation under cathodic bias. Finally, the O 1s spectrum (Fig. 7h) displays a high-energy shoulder ($\sim$533.5 eV), possibly due to the formation of surface hydroxides. These XPS findings are consistent with the observed increase in conductivity, which are primarily attributed to the formation of metallic copper. Furthermore, SEM imaging (Fig. S20) revealed significant morphological degradation of the film after PEC operation, including agglomeration, which aligns with the extensive chemical reduction and loss of structural integrity. The degradation of $CuFeO_2$ under operating conditions is driven by the cathodic reduction of its constituent metal cations. The irreversible

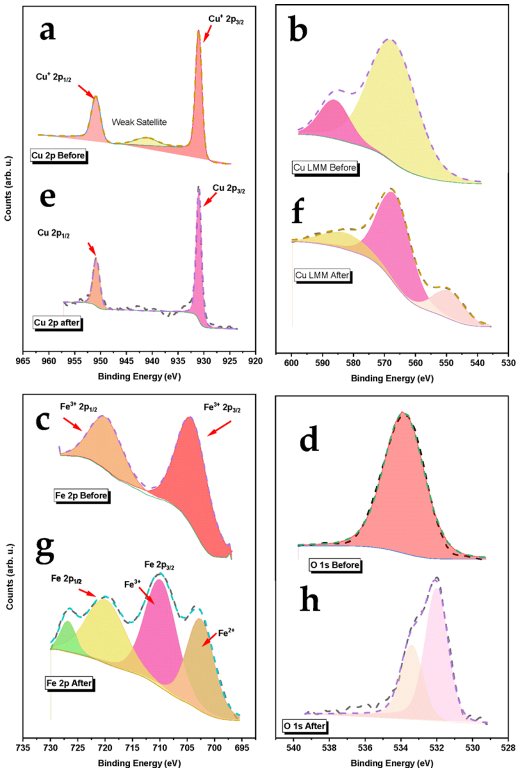

Fig. 7 High-resolution XPS analysis of $CuFeO_2$ before and after PEC operation. (a–d) Region scan spectra of the pristine photocathode: (a) Cu 2p, (b) Cu LMM Auger, (c) Fe 2p, and (d) O 1s regions, confirming the presence of Cu^+, Fe^{3+}, and lattice oxygen. (e–h) Corresponding spectra after PEC testing: (e) Cu 2p and (f) Cu LMM Auger spectra revealing complete reduction to metallic Cu^0; (g) Fe 2p spectrum indicates partial reduction of Fe^{3+} to Fe^{2+}; (h) O 1s spectrum shows the appearance of a new component associated with surface hydroxides/defects. The sample was synthesized hydrothermally at 110 °C for 1 h and annealed at 650 °C for 1 h.

reduction of Cu^+ to Cu^0 and the partial reduction of Fe^{3+} to Fe^{2+} fundamentally alter the electronic structure of the material. The cross-sectional SEM images of the optimized $CuFeO_2$ film before and after HER testing (see Fig. S21) show a continuous, homogeneous film of approximately 1.6 μm thickness with no obvious delamination. The as-deposited and post-operation cross sections therefore appear largely similar, indicating that the macroscopic film architecture remains intact after the 1 h chronoamperometry test and thus the film remains mechanically continuous. Post-catalysis XRD analysis (Fig. S22) further corroborates the XPS and SEM findings. The powder diffraction pattern of the tested $CuFeO_2$ photocathode material reveals the emergence of several new reflections, the majority of which are assigned to Fe_3O_4. Due to the presence of overlapping peaks in the XRD patterns of $CuFeO_2$ and Fe_3O_4, it is challenging to differentiate the $CuFeO_2$ phase solely based on XRD analysis. The presence of Fe_3O_4 is consistent with the XPS-detected reduction of Fe^{3+} to Fe^{2+}. Additionally, weaker reflections corresponding to Cu, Cu_2O, and FeO indicate additional surface redox transformations. Thus, the photocathode undergoes partial phase evolution under operation, dominated by Fe_3O_4 formation. Overall, the post-catalysis characterization suggests that cathodic reduction is likely not concentrated within the surface layer, but rather can propagate into the near-surface region in a manner that degrades electronic pathways without producing substantial through-film delamination. Based on these observations it is proposed that further developments should focus on the suppression of cathodic degradation which should allow for operation with reduced parasitic losses and in turn is expected to increase the H_2 production rate and faradaic efficiency. In this regard, strategies such as co-catalyst modification of the $CuFeO_2$ surface or the formation of heterojunctions are considered suitable. Furthermore, an adapted DoE-guided synthesis approach could be used on the controlled doping of $CuFeO_2$, an aspect that has been excluded from this study, serving as a reliable strategy to further enhance PEC performance.

Conclusion

This study reports the systematic optimization of a one-step hydrothermal synthesis process for $CuFeO_2$ photocathodes fabrication using a Box-Behnken design allowing us to identify hydrothermal temperature and annealing temperature as significant parameters to enhance PEC activity. The optimized photocathodes deliver a photocurrent of -1.7 mA cm^{-2} at +0.4 V *vs.* RHE (N_2-saturated 1 M NaOH), show dual bandgaps (1.58 eV indirect, 3.01 eV direct), exhibiting favourable band alignment and improvements in light-induced interfacial charge transfer. Crucially, we have verified light-driven hydrogen evolution from unmodified $CuFeO_2$ with a steady H_2 production rate of 1.036 μmol h^{-1} using online GC measurements and an average faradaic efficiency of 40%. Post-operation characterization clearly identifies the severe degradation caused by cathodic self-reduction which must be addressed to enable full utilization of $CuFeO_2$ photocathodes. Nevertheless, the optoelectronic and interfacial properties of the as-received bare $CuFeO_2$ appear to be superior and further optimization of $CuFeO_2$ delafossite materials should focus on chemical and interfacial modifications that enhance stability.

Author contributions

M. E. I.: conceptualization, investigation, methodology, formal analysis, data curation, visualization, writing original draft, and writing review & editing. J. P. M.: investigation and methodology. Y. K.: investigation and review. M. A.-L.: supervision, resources, review & editing. L. A. supervision, resources, review & editing. B. T. M: conceptualization, supervision, resources, and writing review & editing.

Conflicts of interest

There are no conflicts to declare.

Data availability

Data for this article, including raw Raman, XRD, XPS, SECM, GC, and photoelectrochemical measurements together with analysis scripts, are available at Figshare at https://doi.org/10.6084/m9.figshare.30521615. The dataset contains files in the following formats: XLSX (Excel spreadsheets), PSM (instrument output), TXT (plain text), PY (Python scripts), DAT (raw measurement files), VMS (instrument-specific data), SFF (spectroscopy files), XY (two-column data), and PNG (figures).

Supplementary information (SI) is available. See DOI: https://doi.org/10.1039/d6ma00088f.

Acknowledgements

M. E. I. would like to thank the DAAD scholarship program ''ERA Fellowships Green Hydrogen'' for their support. L. A and B. M acknowledge support from the LEAP SE program, through the European Project SH2PEC (Horizon 2020, Grant agreement 963530). We also thank the Group of Industrial Chemistry for assistance with sample characterization and for valuable discussions. Special thanks to Wilma Busser and Jonas Hiepel for Raman measurements, Wei Xia for XPS, Patrick Diehl for XRD, Zhangjie Zhai for TEM and Anastasiia Kotova for assistance with the EIS analysis. Deepl.com has been used for grammar and style corrections.

Notes and references

1 D. Zhou, F. Hu, Q. Zhu and Q. Wang, Regional allocation of renewable energy quota in China under the policy of renewable portfolio standards, *Resour., Conserv. Recycl.*, 2022, **176**, 105904.

2 S. D. Tilley, Recent Advances and Emerging Trends in Photo-Electrochemical Solar Energy Conversion, *Adv. Energy Mater.*, 2019, **9**, 1802877.

3 B. Mei, G. Mul and B. Seger, Beyond Water Splitting: Efficiencies of Photo-Electrochemical Devices Producing Hydrogen and Valuable Oxidation Products, *Adv. Sustainable Syst.*, 2017, **1**, 1600035.

4 M. Sun, R.-T. Gao, J. He, X. Liu, T. Nakajima, X. Zhang and L. Wang, Photo-driven Oxygen Vacancies Extends Charge Carrier Lifetime for Efficient Solar Water Splitting, *Angew. Chem.*, 2021, **60**, 17601–17607.

5 S. Hu, C. Xiang, S. Haussener, A. D. Berger and N. S. Lewis, An analysis of the optimal band gaps of light absorbers in integrated tandem photoelectrochemical water-splitting systems, *Energy Environ. Sci.*, 2013, **6**, 2984.

6 M. S. Prévot and K. Sivula, Photoelectrochemical Tandem Cells for Solar Water Splitting, *J. Phys. Chem. C*, 2013, **117**, 17879–17893.

7 B. Seger, I. E. Castelli, P. C. K. Vesborg, K. W. Jacobsen, O. Hansen and I. Chorkendorff, 2-Photon tandem device for water splitting: comparing photocathode first versus photoanode first designs, *Energy Environ. Sci.*, 2014, **7**, 2397–2413.

8 B. A. Pinaud, J. D. Benck, L. C. Seitz, A. J. Forman, Z. Chen, T. G. Deutsch, B. D. James, K. N. Baum, G. N. Baum, S. Ardo, H. Wang, E. Miller and T. F. Jaramillo, Technical and economic feasibility of centralized facilities for solar hydrogen production via photocatalysis and photoelectrochemistry, *Energy Environ. Sci.*, 2013, **6**, 1983.

9 J. Luo, S. D. Tilley, L. Steier, M. Schreier, M. T. Mayer, H. J. Fan and M. Grätzel, Solution transformation of Cu_2O into $CuInS_2$ for solar water splitting, *Nano Lett.*, 2015, **15**, 1395–1402.

10 Q. Wang, T. Hisatomi, Q. Jia, H. Tokudome, M. Zhong, C. Wang, Z. Pan, T. Takata, M. Nakabayashi, N. Shibata, Y. Li, I. D. Sharp, A. Kudo, T. Yamada and K. Domen, Scalable water splitting on particulate photocatalyst sheets with a solar-to-hydrogen energy conversion efficiency exceeding 1%, *Nat. Mater.*, 2016, **15**, 611–615.

11 Q. Wang, T. Hisatomi, Y. Suzuki, Z. Pan, J. Seo, M. Katayama, T. Minegishi, H. Nishiyama, T. Takata, K. Seki, A. Kudo, T. Yamada and K. Domen, Particulate Photocatalyst Sheets Based on Carbon Conductor Layer for Efficient Z-Scheme Pure-Water Splitting at Ambient Pressure, *J. Am. Chem. Soc.*, 2017, **139**, 1675–1683.

12 A. Milbrat, W. Vijselaar, Y. Guo, B. Mei, J. Huskens and G. Mul, Integration of Molybdenum-Doped, Hydrogen-Annealed $BiVO_4$ with Silicon Microwires for Photoelectrochemical Applications, *ACS Sustainable Chem. Eng.*, 2019, **7**, 5034–5044.

13 Y. J. Jang, I. Jeong, J. Lee, J. Lee, M. J. Ko and J. S. Lee, Unbiased Sunlight-Driven Artificial Photosynthesis of Carbon Monoxide from CO_2 Using a ZnTe-Based Photocathode and a Perovskite Solar Cell in Tandem, *ACS Nano*, 2016, **10**, 6980–6987.

14 Y. J. Jang, J. Ryu, D. Hong, S. Park and J. S. Lee, A multistacked hyperporous silicon flake for highly active solar hydrogen production, *Chem. Commun.*, 2016, **52**, 10221–10224.

15 J. Y. Kim, G. Magesh, D. H. Youn, J.-W. Jang, J. Kubota, K. Domen and J. S. Lee, Single-crystalline, wormlike hematite photoanodes for efficient solar water splitting, *Sci. Rep.*, 2013, **3**, 2681.

16 A. Paracchino, V. Laporte, K. Sivula, M. Grätzel and E. Thimsen, Highly active oxide photocathode for photoelectrochemical water reduction, *Nat. Mater.*, 2011, **10**, 456–461.

17 X. Shi, I. Y. Choi, K. Zhang, J. Kwon, D. Y. Kim, J. K. Lee, S. H. Oh, J. K. Kim and J. H. Park, Efficient photoelectrochemical hydrogen production from bismuth vanadate-decorated tungsten trioxide helix nanostructures, *Nat. Commun.*, 2014, **5**, 4775.

18 S. D. Tilley, M. Schreier, J. Azevedo, M. Stefik and M. Graetzel, Ruthenium Oxide Hydrogen Evolution Catalysis on Composite Cuprous Oxide Water-Splitting Photocathodes, *Adv. Funct. Mater.*, 2014, **24**, 303–311.

19 Z. Zhang, R. Dua, L. Zhang, H. Zhu, H. Zhang and P. Wang, Carbon-layer-protected cuprous oxide nanowire arrays for efficient water reduction, *ACS Nano*, 2013, **7**, 1709–1717.

20 M. Moriya, T. Minegishi, H. Kumagai, M. Katayama, J. Kubota and K. Domen, Stable hydrogen evolution from CdS-modified $CuGaSe_2$ photoelectrode under visible-light irradiation, *J. Am. Chem. Soc.*, 2013, **135**, 3733–3735.

21 X. Wen, W. Luo and Z. Zou, Photocurrent improvement in nanocrystalline Cu_2ZnSnS_4 photocathodes by introducing porous structures, *J. Mater. Chem. A*, 2013, **1**, 15479.

22 L. Rovelli, S. D. Tilley and K. Sivula, Optimization and stabilization of electrodeposited Cu_2ZnSnS_4 photocathodes for solar water reduction, *ACS Appl. Mater. Interfaces*, 2013, **5**, 8018–8024.

23 P. Dai, J. Xie, M. T. Mayer, X. Yang, J. Zhan and D. Wang, Solar hydrogen generation by silicon nanowires modified with platinum nanoparticle catalysts by atomic layer deposition, *Angew. Chem.*, 2013, **52**, 11119–11123.

24 B. Seger, T. Pedersen, A. B. Laursen, P. C. K. Vesborg, O. Hansen and I. Chorkendorff, Using TiO_2 as a conductive protective layer for photocathodic H_2 evolution, *J. Am. Chem. Soc.*, 2013, **135**, 1057–1064.

25 N. P. Dasgupta, C. Liu, S. Andrews, F. B. Prinz and P. Yang, Atomic layer deposition of platinum catalysts on nanowire surfaces for photoelectrochemical water reduction, *J. Am. Chem. Soc.*, 2013, **135**, 12932–12935.

26 A. Scheid, Q. Song, S. Ribet, C. Ophus, Y. E. Suyolcu, D. G. Schlom, T. Heil and P. A. van Aken, Atomic-Scale Mechanisms of Nucleation and Stabilization in $CuCrO_2$ and $CuFeO_2$ Delafossite Thin Films on Al_2O_3, *Adv. Mater. Inter.*, 2025, **12**, 2500218.

27 S. Saadi, A. Bouguelia and M. Trari, Photocatalytic hydrogen evolution over $CuCrO_2$, *Sol. Energy*, 2006, **80**, 272–280.

28 I. Herraiz-Cardona, F. Fabregat-Santiago, A. Renaud, B. Julián-López, F. Odobel, L. Cario, S. Jobic and S. Giménez, Hole conductivity and acceptor density of p-type $CuGaO_2$

nanoparticles determined by impedance spectroscopy: The effect of Mg doping, *Electrochim. Acta*, 2013, **113**, 570–574.

29 C. G. Read, Y. Park and K.-S. Choi, Electrochemical Synthesis of p-Type $CuFeO_2$ Electrodes for Use in a Photoelectrochemical Cell, *J. Phys. Chem. Lett.*, 2012, **3**, 1872–1876.

30 M. El Idrissi, B. Mei, M. Abd-Lefdil and L. Atourki, Making Solar Hydrogen: A Review of the Challenges and Strategies of Synthesizing $CuFeO_2$ Photocathodes for Photoelectrochemical Water Splitting, *Molecules*, 2025, **30**, 1152.

31 S. Ardo, D. Fernandez Rivas, M. A. Modestino, V. Schulze Greiving, F. F. Abdi, E. Alarcon Llado, V. Artero, K. Ayers, C. Battaglia, J.-P. Becker, D. Bederak, A. Berger, F. Buda, E. Chinello, B. Dam, V. Di Palma, T. Edvinsson, K. Fujii, H. Gardeniers, H. Geerlings, S. M. H. Hashemi, S. Haussener, F. Houle, J. Huskens, B. D. James, K. Konrad, A. Kudo, P. P. Kunturu, D. Lohse, B. Mei, E. L. Miller, G. F. Moore, J. Muller, K. L. Orchard, T. E. Rosser, F. H. Saadi, J.-W. Schüttauf, B. Seger, S. W. Sheehan, W. A. Smith, J. Spurgeon, M. H. Tang, R. van de Krol, P. C. K. Vesborg and P. Westerik, Pathways to electrochemical solar-hydrogen technologies, *Energy Environ. Sci.*, 2018, **11**, 2768–2783.

32 Y. Cheng, S. Li, H. Li, D. Meng, S. Zhang, M. Qing, M. Pan, F. Yang, C. Wang, L. Li, G. Liu, P. Qin, C. Liu, H. Song, H. Feng, H. Chen, J. Li, C.-L. Liu, N. Tsubaki and W.-S. Dong, $CuFeO_2$ Integrated with Orderly Stacked Multilamellar ZSM-5 Nanosheets for Highly Active and Selective Synthesis of Aromatics from CO_2 Hydrogenation, *ACS Catal.*, 2025, **15**, 15706–15721.

33 R.-P. Li, S.-M. Yu and Z.-Y. Zhao, Facet engineering for improved carrier separation and transport in $CuFeO_2$ photocathodes, *Mater. Chem. Phys.*, 2024, **311**, 128582.

34 S. Bassaid, M. Chaib, S. Omeiri, A. Bouguelia and M. Trari, Photocatalytic reduction of cadmium over $CuFeO_2$ synthesized by sol–gel, *J. Photochem. Photobiol., A*, 2009, **201**, 62–68.

35 S. Kato, R. Fujimaki, M. Ogasawara, T. Wakabayashi, Y. Nakahara and S. Nakata, Oxygen storage capacity of $CuMO_2$ (M = Al, Fe, Mn, Ga) with a delafossite-type structure, *Appl. Catal., B*, 2009, **89**, 183–188.

36 W. Ketir, A. Bouguelia and M. Trari, NO_3^- removal with a new delafossite $CuCrO_2$ photocatalyst, *Desalination*, 2009, **244**, 144–152.

37 S. Zhou, X. Fang, Z. Deng, D. Li, W. Dong, R. Tao, G. Meng and T. Wang, Room temperature ozone sensing properties of p-type $CuCrO_2$ nanocrystals, *Sens. Actuators, B*, 2009, **143**, 119–123.

38 C. J. Dong, W. X. Yu, M. Xu, J. J. Cao, Y. Zhang, Y. H. Chuai and Y. D. Wang, Evidence of room temperature ferromagnetism in Co-doped transparent $CuAlO_2$ semiconductor, *J. Alloys Compd.*, 2012, **512**, 195–198.

39 C. Gao, F. Lin, X. Zhou, W. Shi and A. Liu, Fe concentration dependences of microstructure and magnetic properties for $Cu(Cr_{1-x}Fe_x)O_2$ ceramics, *J. Alloys Compd.*, 2013, **565**, 154–158.

40 F. Lin, W. Shi and A. Liu, Optical bandgap modulation and magnetic characterization of Fe-doped $CuCrO_2$ nanopowders, *J. Alloys Compd.*, 2012, **529**, 21–24.

41 B. Ling, J. L. Zhao, X. W. Sun, S. T. Tan, A. K. K. Kyaw, Y. Divayana and Z. L. Dong, Color tunable light-emitting diodes based on p^+-Si/p-$CuAlO_2$/n-ZnO nanorod array heterojunctions, *Appl. Phys. Lett.*, 2010, **97**, 013101.

42 A. S. Reddy, H.-H. Park, G. M. Rao, S. Uthanna and P. S. Reddy, Effect of substrate temperature on the physical properties of dc magnetron sputtered $CuAlO_2$ films, *J. Alloys Compd.*, 2009, **474**, 401–405.

43 H. F. Jiang, H. C. Lei, X. B. Zhu, G. Li, Z. R. Yang, W. H. Song, J. M. Dai, Y. P. Sun and Y. K. Fu, Effects of citric acid on properties of single phase $CuAlO_2$ thin films derived by chemical solution deposition, *J. Alloys Compd.*, 2009, **487**, 404–408.

44 M. S. Prévot, X. A. Jeanbourquin, W. S. Bourée, F. Abdi, D. Friedrich, R. van de Krol, N. Guijarro, F. Le Formal and K. Sivula, Evaluating Charge Carrier Transport and Surface States in $CuFeO_2$ Photocathodes, *Chem. Mater.*, 2017, **29**, 4952–4962.

45 M. S. Prévot, N. Guijarro and K. Sivula, Enhancing the Performance of a robust sol-gel-processed p-type delafossite $CuFeO_2$ photocathode for solar water reduction, *ChemSusChem*, 2015, **8**, 1359–1367.

46 S. Omeiri, B. Bellal, A. Bouguelia, Y. Bessekhouad and M. Trari, Electrochemical and photoelectrochemical characterization of $CuFeO_2$ single crystal, *J. Solid State Electrochem.*, 2009, **13**, 1395–1401.

47 M. A. Marquardt, N. A. Ashmore and D. P. Cann, Crystal chemistry and electrical properties of the delafossite structure, *Thin Solid Films*, 2006, **496**, 146–156.

48 R. Präg, M. Kölbach, F. F. Abdi, I. Y. Ahmet, M. Schleuning, D. Friedrich and R. van de Krol, Photoelectrochemical Properties of $CuFeO_2$ Photocathodes Prepared by Pulsed Laser Deposition, *Chem. Mater.*, 2024, **36**(16), 7764–7780.

49 M. S. Prévot, Y. Li, N. Guijarro and K. Sivula, Improving charge collection with delafossite photocathodes: a host–guest $CuAlO_2$/$CuFeO_2$ approach, *J. Mater. Chem. A*, 2016, **4**, 3018–3026.

50 J. Gu, A. Wuttig, J. W. Krizan, Y. Hu, Z. M. Detweiler, R. J. Cava and A. B. Bocarsly, Mg-Doped $CuFeO_2$ Photocathodes for Photoelectrochemical Reduction of Carbon Dioxide, *J. Phys. Chem. C*, 2013, **117**, 12415–12422.

51 D. Xiong, Y. Qi, X. Li, X. Liu, H. Tao, W. Chen and X. Zhao, Hydrothermal synthesis of delafossite $CuFeO_2$ crystals at 100 °C, *RSC Adv.*, 2015, **5**, 49280–49286.

52 A. P. Amrute, Z. Łodziana, C. Mondelli, F. Krumeich and J. Pérez-Ramírez, Solid-State Chemistry of Cuprous Delafossites: Synthesis and Stability Aspects, *Chem. Mater.*, 2013, **25**, 4423–4435.

53 Z. Deng, X. Fang, S. Wu, Y. Zhao, W. Dong, J. Shao and S. Wang, Structure and optoelectronic properties of Mg-doped $CuFeO_2$ thin films prepared by sol–gel method, *J. Alloys Compd.*, 2013, **577**, 658–662.

54 C.-Q. Guo, H.-S. Zheng, J. Yang, X. Xiang and Z.-Y. Zhao, Photocatalytic-Fenton synergistic reaction of $CuFeO_2$/Fe_2O_3 heterostructure for tetracycline hydrochloride degradation, *Appl. Surf. Sci.*, 2025, **685**, 162063.

55 Q.-L. Liu, Z.-Y. Zhao, R.-D. Zhao and J.-H. Yi, Fundamental properties of delafossite $CuFeO_2$ as photocatalyst for solar energy conversion, *J. Alloys Compd.*, 2020, **819**, 153032.

56 M. Ito, C. Izawa and T. Watanabe, Direct Fabrication of a $CuFeO_2$/Fe Photocathode for Solar Hydrogen Production by Hydrothermal Method, *Chem. Lett.*, 2017, **46**, 814–816.

57 Y. J. Jang, Y. B. Park, H. E. Kim, Y. H. Choi, S. H. Choi and J. S. Lee, Oxygen-Intercalated $CuFeO_2$ Photocathode Fabricated by Hybrid Microwave Annealing for Efficient Solar Hydrogen Production, *Chem. Mater.*, 2016, **28**, 6054–6061.

58 M. Ferri, J. D. Elliott, M. F. Camellone, S. Fabris and S. Piccinin, $CuFeO_2$–Water Interface under Illumination: Structural, Electronic, and Catalytic Implications for the Hydrogen Evolution Reaction, *ACS Catal.*, 2021, **11**, 1897–1910.

59 T. Shinagawa, W. Tachibori, T. Nishii and A. Ohtaka, One-pot hydrothermal synthesis of orientated delafossite $CuFeO_2$ films from a mildly acidic solution on substrates, *J. Mater. Chem. C*, 2023, **11**, 8616–8625.

60 H. Xu, R. Wu, J.-Y. Zhang, W. Han, L. Chen, X. Liang, C. Y. Haw, P. Mazzolini, O. Bierwagen, D.-C. Qi and K. H. L. Zhang, Revealing the Electronic Structure and Optical Properties of $CuFeO_2$ as a p-Type Oxide Semiconductor, *ACS Appl. Electron. Mater.*, 2021, **3**, 1834–1841.

61 S. R. Nersesyan and S. G. Petrosyan, Depletion length and space charge layer capacitance in doped semiconductor nanoshpere, *Semicond. Sci. Technol.*, 2012, **27**, 125009.

62 Y. Hermans, A. Klein, H. P. Sarker, M. N. Huda, H. Junge, T. Toupance and W. Jaegermann, Pinning of the Fermi Level in $CuFeO_2$ by Polaron Formation Limiting the Photovoltage for Photochemical Water Splitting, *Adv. Funct. Materials*, 2020, **30**, 1910432.